IEEE Access
Multidisciplinary | Rapid Review | Open Access Journal

Date of publication xxxx 00, 0000, date of current version xxxx 00, 0000.

Digital Object Identifier 10.1109/ACCESS.2017.Doi Number

Rotor-position Detection in Permanent-magnet Wheel Motor to Ensure Smooth Startup from Standstill

Kewang Qu[1], Weili Li[1,*], Guoqing Xu[2], Junci Cao[1*], T. X Mei[3], Yihuang Zhang[1] and Hao Hu[4]

[1]School of Electrical Engineering, Beijing Jiaotong University, 100044 P. R. China
[2]School of Mechatronic Engineering and Automation, Shanghai University, 200444, P. R. China
[3]School of Computing, Science and Engineering, University of Salford, M5 4WT, Salford, UK
[4]Institute of Rail Transit, Tongji University, Shanghai 201804, P. R. China

*Corresponding Author/E-mail: Wlli@bjtu.edu.cn, jccao@bjtu.edu.cn; Tel.: +86-136-7587-1232

This work is supported by National Natural Science Foundation of China under Grant U61603377 and U51577007.

ABSTRACT In this paper, an innovative rotor-position-detection method for a permanent-magnet wheel motor (PMWM) that operates from standstill to low speed is presented. The neutral voltage, which is sensed through phase-shifted pulse width modulation, overcomes the limitations of the conventional back electromotive force (EMF)-based position-detection method, which is more suitable for high-speed operation. In addition, a technique that ensures a transition between the two position-detection methods is presented to cover the full speed range. Computer simulations are employed to design and assess the neutral-voltage-based and EMF-based position-detection methods. The results of the position detection and angle error are presented starting from standstill to low speed. A step current (i_q) corresponding to motor torque demand is applied for the starting process in the two position-detection methods. The experimental studies of the new position-detection method are conducted. The method is successfully applied to drive a 60-kW PMWM that operates from standstill to high speed. This demonstrates the effectiveness and performance of the presented method.

INDEX TERMS machine vector control, position detection, pulse width modulation EMF, sensorless control saliencies

I. INTRODUCTION

The sensorless operations of permanent-magnet synchronous motors (PMSMs) have been extensively studied in the past two decades. PMSMs are currently used in numerous electric vehicles (EVs), tram applications, air conditioners and cooling pumps. However, limitations still exist, and PMSMs cannot cover universal EV and tram traction applications despite recent important progress.

Studies on sensorless position-detection for PMSMs have focused on developing reliable detection methods that reduce the cost of position transducers because their application cost and structure are complex [1]. No single sensorless position-detection method is suitable for all types of motor controls or all operating conditions. Techniques for the back electromotive force (EMF) of PMSMs that allow for high-performance control from medium to high speed have been presented. The rotor position is estimated using sensorless position-detection techniques by observing the phase current and stator voltages of an electrical motor in the *d–q* axis frame [2-3].

The back EMF position-detection method is the simplest method, and it is suitable for high speed. Although new methods, such as the Kalman filter and extended Kalman filter, extend the application range of the back EMF method to low speed, they do not work at extremely low speed because of the small back EMF and their sensitivity to measurement noise and motor parameter errors [4–6]. New methods based on the virtual third harmonic back EMF and the second-order generalized integral rotor flux are used to improve the precision of position estimation [7–8].

The recently proposed signal-injection (sinusoidal voltage injection and square-wave voltage injection) method is suitable for interior PMSMs with salient rotors. This method injects signal into the stator voltage or current. A special method is required to process the signal to separate the effective signal from noise. This increases the complexity of the position-detection method [9–20].

A few methods have been investigated to reduce the estimated harmonic error, such as adaptive filters and sliding-mode observers [21–30]. However, these methods are not capable of surface PMSM (SPMSM) position detection from standstill to extremely low speed because of the considerably small saliency.

Position detection at standstill and low speed has been proposed [32–35] based on carrier phase-shift pulse width modulation (PWM), and research has been conducted on transient-signal analysis based on phase-shift PWM in a PMSM inverter. In addition, rotor magnet polarity identification in the *d*–*q* axis frame using pulse voltage has been analyzed in detail by modeling the flux linkage saturation effect on the *d* axis.

In the present paper, a novel rotor-position scheme is proposed for traction operation in tram applications. The proposed scheme exploits the more precise initial rotor position at standstill unlike the approach used in the conventional method. In the proposed position-detection method, the rotor position and its angle error at low and high speeds were simulated using MATLAB. A solution to achieve a shift between the two different position-detection methods is also presented in this paper. Moreover, the experimental result presented in the final section verifies the validity of the proposed method.

The remainder of the paper is structured as follows: Section II provides a detailed description of the novel neutral-voltage scheme, including at low speed and standstill. Section III discusses the simulation at low speed, and the effect of back EMF. Section IV describes the test setup of a wheel motor for tram applications as well as the control and experimental results of the proposed sensorless scheme. Finally, Section V provides the conclusion drawn from the study.

II. PROPOSED NEUTRAL-VOLTAGE SCHEME

A. APPLICATION OF PHASE-SHIFTED PWM TECHNOLOGY TO POSITION DETECTION

Rotor position cannot be detected using SPMSM EMF, which is extremely small at standstill or low speed. The equation for an SPMSM is expressed using its resistance and inductance. Six transient states occur in one PWM period from carrier phase-shift PWM and neutral voltage. The self and mutual inductances of an SPMSM contain position information regarding the SPMSM rotor. By substituting the self and mutual inductances into phase-voltage equations, a strong correlation can be found between the motor position and the neutral-point voltage. These equations also show the saliency of the self and mutual inductances because their frequency is twice the electrical fundamental frequency. Simultaneously, the rotor magnet polarity identification in the *d*–*q*-axis frame is presented in detail by modeling the flux-linkage saturation effect on the *d* axis [32–35]. The effect of EMF on position detection increases with rotor speed; thus, further investigation was performed. Furthermore, a transfer method that achieves transition between the two different position-detection methods at low and high speeds is developed to ensure smooth operation.

The standard inverter and motor stator equivalent circuit for SPMSM is shown in Fig 1A. Variations in the on/off PWM switching pulse for the three phases results in six different circuit configurations in each PWM period, where the duty cycles are determined by control algorithms. Figure 1B gives three phase-shifted PWM carrier waves and logic for phase *A*, phase *B*, and phase *C* of the SPMSM motor, respectively.

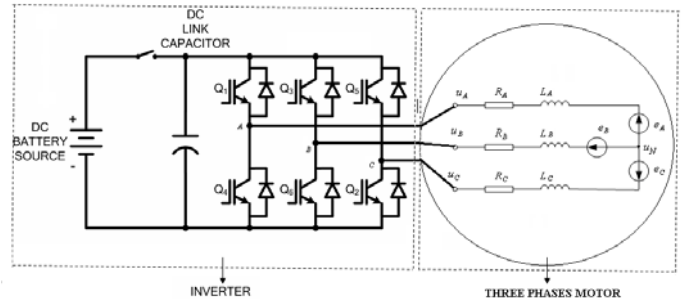

FIGURE 1A. Standard inverter and Motor stator equivalent circuit

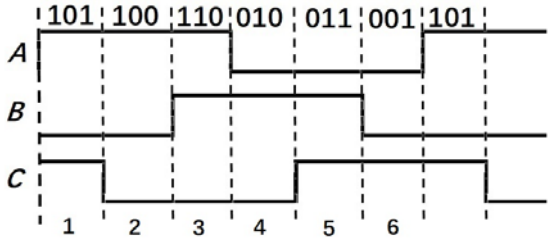

FIGURE 1B. Logic of the three phases of carrier phase shifted PWM

In each PWM period, the rising edge of the phase shifted PWM pulse results in three different circuit configurations in transient conditions. The equivalent circuits of state 5(phases *B* and *C* are connected to the positive DC bus and phase *A* to the negative), state 1(phases *A* and *C* are connected to the positive DC bus and phase *B* to the negative) and state 3(phases *A* and *B* are connected to the positive DC bus and phase *C* to the negative) are shown in Fig 1C. Neutral voltage measurement (V_N) was obtained shortly after each of the rising edge of PWM. Three measurements, namely V_{AN}, V_{BN}, and V_{CN} were obtained in one PWM cycle.

At standstill and low speed, the back EMFs were neglected. A sample of the neutral voltage was obtained at the rising edge of PWM in the transient response of the motor windings. The voltage across the winding resistance was neglected as the time is not 100 times less than the time constant.

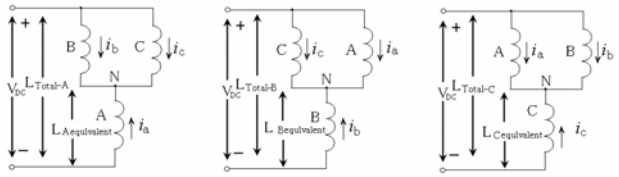

FIGURE 1C. Equivalent circuits of different states.

A detailed analysis of state 5 is presented. According to the voltage law, the decoupled equations of the three phases are given as (1)-(3).

$$V_{AN} = L_a \frac{di_a}{dt} + M_{ab} \frac{di_b}{dt} + M_{ac} \frac{di_c}{dt} \qquad (1)$$

$$V_{BN} = M_{ab}\frac{di_a}{dt} + L_b\frac{di_b}{dt} + M_{bc}\frac{di_c}{dt} \quad (2)$$

$$V_{CN} = M_{ac}\frac{di_a}{dt} + M_{bc}\frac{di_b}{dt} + L_c\frac{di_c}{dt} \quad (3)$$

where L_a, L_b, L_c are the self-inductances of phase *A*, phase *B* and phase *C; M_{ab}, M_{ac}, M_{bc}* are the mutual inductances between phase *A,* phase *B* and phase *C; V_{AN}, V_{BN}, V_{CN}* are the voltages of phase *A,* phase *B* and phase *C;*

According to the current law, the current equations are given as (4)-(6), since the total current through the neutral point is zero.

$$i_a + i_b + i_c = 0 \quad (4)$$

$$i_c = -i_a - i_b \quad (5)$$

$$i_b = -i_a - i_c \quad (6)$$

where i_a, i_b, and i_c are the currents of phase *A*, phase *B*, and phase *C*.

It is clear that V_{CN} (voltage of phase *C*) is equal to V_{BN} (voltage of phase *B*) as phases *B* and *C* are connected to positive DC bus and neutral point.

$$V_{CN} = V_{BN} \quad (7)$$

Equation (8) is obtained by substituting (2) and (3) into (7).

$$(M_{ac} - M_{ab})\frac{di_a}{dt} + (M_{bc} - L_b)\frac{di_b}{dt} + (L_c - M_{bc})\frac{di_c}{dt} = 0 \quad (8)$$

Equation (9) is obtained by substituting (5) into (8).

$$\frac{di_b}{dt} = -\frac{M_{ab} - M_{ac} - M_{bc} + L_c}{L_c - 2M_{bc} + L_b}\frac{di_a}{dt} \quad (9)$$

Substituting (6) into (8) gives

$$\frac{di_c}{dt} = \frac{M_{ab} - M_{ac} + M_{bc} - L_b}{L_c - 2M_{bc} + L_b}\frac{di_a}{dt} \quad (10)$$

The voltage of phase A is expressed as (11) with the equivalent inductance of phase A ($L_{A\text{-}Equivalent}$).

$$V_{AN} = L_{A-Equivalent}\left(\frac{di_a}{dt}\right) \quad (11)$$

According to (9), (10), (11), and (1), $L_{A\text{-}Equivalent}$ can be derived as

$$L_{A-Equivalent} = L_a + \frac{M_{ab}(M_{bc} + M_{ac} - M_{ab} - L_c) + M_{ac}(M_{ab} + M_{bc} - M_{ac} - L_b)}{L_c - 2M_{bc} + L_b} \quad (12)$$

Similar analyses are performed on state 1 and state 3 for the other two phases to obtain equations (13)-(14) as follows:

$$L_{B-Equivalent} = L_b + \frac{M_{ab}(M_{bc} + M_{ac} - M_{ab} - L_c) + M_{bc}(M_{ab} + M_{ac} - M_{bc} - L_a)}{L_a - 2M_{ac} + L_c} \quad (13)$$

$$L_{C-Equivalent} = L_c + \frac{M_{ac}(M_{ab} + M_{bc} - M_{ac} - L_b) + M_{bc}(M_{ab} + M_{ac} - M_{bc} - L_a)}{L_a - 2M_{ab} + L_b} \quad (14)$$

where $L_{B\text{-}Equivalent}$ and $L_{C\text{-}Equivalent}$ are the equivalent inductances of phase *B* and phase *C*;

The DC bus voltage in state 5 can be obtained as show in (15).

$$V_{DC} = V_{AN} - V_{BN} \quad (15)$$

where V_{DC} is the DC bus voltage of the inverter.

The DC bus voltage is expressed with the time derivation of phase A current and relative total inductance ($L_{Total\text{-}A}$) as given in (16).

$$V_{DC} = L_{Total-A}\left(\frac{di_a}{dt}\right) \quad (16)$$

Substituting (9) and (10) into (1) and (2), then substituting them into (16), the $L_{Total-A}$ can be derived as given in (17).

$$L_{Total-A} = (L_a - M_{ab} - M_{ac} + M_{bc}) + \frac{(L_b - M_{ab} - M_{bc} + M_{ac})(L_c - M_{bc} - M_{ac} + M_{ab})}{(L_b - 2M_{bc} + L_c)} \quad (17)$$

Similar analyses were performed for state 1 and state 3 for the other two phases to obtain equations (18)-(19) as follows:

$$L_{Total-B} = (L_b - M_{ab} - M_{bc} + M_{ac}) + \frac{(L_a - M_{ab} - M_{ac} + M_{bc})(L_c - M_{bc} - M_{ac} + M_{ab})}{(L_a - 2M_{ac} + L_c)} \quad (18)$$

$$L_{Total-C} = (L_c - M_{bc} - M_{ac} + M_{ab}) + \frac{(L_a - M_{ab} - M_{ac} + M_{bc})(L_b - M_{ab} - M_{bc} + M_{ac})}{(L_a - 2M_{ab} + L_b)} \quad (19)$$

where $L_{Total\text{-}B}$ and $L_{Total\text{-}C}$ are the relative total inductances of phase *B* and phase *C*.

The measured neutral point voltages relative to the DC bus voltage can be expressed as given in (20)-(22).

$$\overline{A} = \frac{-V_{AN}}{V_{DC}} = \frac{L_{A-Equivalent}}{L_{Total-A}} \quad (20)$$

$$\overline{B} = \frac{-V_{BN}}{V_{DC}} = \frac{L_{B-Equivalent}}{L_{Total-B}} \quad (21)$$

$$\overline{C} = \frac{-V_{CN}}{V_{DC}} = \frac{L_{C-Equivalent}}{L_{Total-C}} \quad (22)$$

For further theoretical study, the variations of the inductance with the motor position can be expressed using sinusoidal approximations as in the following equations (23)-(28). Equations (23)-(28) reveal the saliency of the self and mutual inductances because the frequency is twice the rotor frequency.

$$L_a = L_s - L_{sl}\cos 2\theta \tag{23}$$

$$L_b = L_s - L_{sl}\cos(2\theta + 120^o) \tag{24}$$

$$L_c = L_s - L_{sl}\cos(2\theta - 120^o) \tag{25}$$

$$M_{ab} = M_s + M_{sl}\cos(2\theta - 120^o) \tag{26}$$

$$M_{bc} = M_s + M_{sl}\cos(2\theta) \tag{27}$$

$$M_{ac} = M_s + M_{sl}\cos(2\theta + 120^o) \tag{28}$$

where L_s and M_s are the constants of the self and mutual inductances, respectively. L_{sl} and M_{sl} are the amplitudes of the second-harmonic element of the self and mutual inductances, respectively. θ is the angle between phase-A and d axes, as shown in Fig. 2.

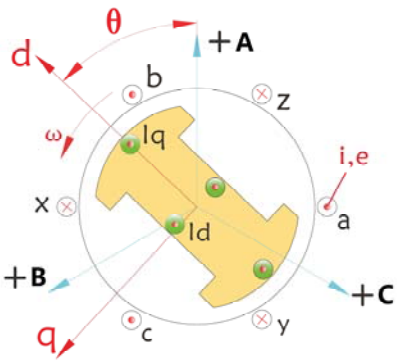

FIGURE 2. **Position relationship between the phase-A and d axes.**

Substituting (23)-(28) into (12), $L_{A\text{-}Equivalent}$ can be obtained as

$$\begin{aligned} L_{A-Equivalent} &= L_s + 2M_s - (M_{sl} + L_{sl})\cos(2\theta) \\ &+ \frac{-2M_sL_s - M_sL_s\cos(2\theta) + L_sM_{sl}\cos(2\theta) + 2M_{sl}L_{sl}\cos^2(2\theta) - \frac{3}{2}M_{sl}L_{sl}}{2L_s + 2M_s + L_{sl}\cos(2\theta) + 2M_{sl}\cos(2\theta)} \\ &+ \frac{-2M_s^2 - M_sM_{sl}\cos(2\theta) + 4M_{sl}\cos^2(2\theta) - 3M_{sl}^2}{2L_s + 2M_s + L_{sl}\cos(2\theta) + 2M_{sl}\cos(2\theta)} \end{aligned} \tag{29}$$

Equation (29) can be rearranged as given below

$$\begin{aligned} L_{A-Equivalent} &= \frac{(2L_s^2 + 4M_sL_s - \frac{3}{2}M_{sl}L_{sl} + 2M_s^2 - 3M_{sl}^2)}{2(L_s + M_s) + (L_{sl} + 2M_{sl})\cos(2\theta)} \\ &+ \frac{[(M_s + L_s)(M_{sl} - L_{sl})]\cos(2\theta)}{2(L_s + M_s) + (L_{sl} + 2M_{sl})\cos(2\theta)} \\ &+ \frac{[(2M_{sl} + L_{sl})(M_{sl} - L_{sl})]\cos^2(2\theta)}{2(L_s + M_s) + (L_{sl} + 2M_{sl})\cos(2\theta)} \end{aligned} \tag{30}$$

Similar analyses were performed for $L_{B\text{-}Equivalent}$ and $L_{C\text{-}Equivalent}$ as given in (31) and (32)

$$\begin{aligned} L_{B-Equivalent} &= \frac{(2L_s^2 + 4M_sL_s - \frac{3}{2}M_{sl}L_{sl} + 2M_s^2 - 3M_{sl}^2)}{2(L_s + M_s) + (L_{sl} + 2M_{sl})\cos(2\theta + 120^0)} + \\ &\frac{[(M_s + L_s)(M_{sl} - L_{sl})]\cos(2\theta + 120^0)}{2(L_s + M_s) + (L_{sl} + 2M_{sl})\cos(2\theta + 120^0)} + \\ &\frac{[(2M_{sl} + L_{sl})(M_{sl} - L_{sl})]\cos^2(2\theta + 120^0)}{2(L_s + M_s) + (L_{sl} + 2M_{sl})\cos(2\theta + 120^0)} \end{aligned} \tag{31}$$

$$\begin{aligned} L_{C-Equivalent} &= \frac{(2L_s^2 + 4M_sL_s - \frac{3}{2}M_{sl}L_{sl} + 2M_s^2 - 3M_{sl}^2)}{2(L_s + M_s) + (L_{sl} + 2M_{sl})\cos(2\theta - 120^0)} + \\ &\frac{[(M_s + L_s)(M_{sl} - L_{sl})]\cos(2\theta - 120^0)}{2(L_s + M_s) + (L_{sl} + 2M_{sl})\cos(2\theta - 120^0)} + \\ &\frac{[(2M_{sl} + L_{sl})(M_{sl} - L_{sl})]\cos^2(2\theta - 120^0)}{2(L_s + M_s) + (L_{sl} + 2M_{sl})\cos(2\theta - 120^0)} \end{aligned} \tag{32}$$

Substituting (23)-(28) into (17), $L_{Total\text{-}A}$ can be obtained as

$$\begin{aligned} L_{Total-A} &= L_s + M_s - (L_{sl} + 2M_{sl})\cos(2\theta) \\ &+ \frac{(L_s + M_s)^2 + (L_s + M_s)(2M_{sl} + L_{sl})\cos(2\theta)}{2L_s + 2M_s + L_{sl}\cos(2\theta) + 2M_{sl}\cos(2\theta)} \\ &+ \frac{(2M_{sl} + L_{sl})^2\cos^2(2\theta) - \frac{3}{4}(2M_{sl} + L_{sl})^2}{2L_s + 2M_s + L_{sl}\cos(2\theta) + 2M_{sl}\cos(2\theta)} \end{aligned} \tag{33}$$

Equation (33) can be rearranged as given below

$$L_{Total-A} = \frac{3(L_s + M_s)^2 - \frac{3}{4}(2M_{sl} + L_{sl})^2}{2(L_s + M_s) + (L_{sl} + 2M_{sl})\cos(2\theta)} \tag{34}$$

Similar analyses were performed for $L_{B\text{-}Equivalent}$ *and* $L_{C\text{-}Equivalent}$ as given in (35) and (36)

$$L_{Total-B} = \frac{3(L_s + M_s)^2 - \frac{3}{4}(2M_{sl} + L_{sl})^2}{2(L_s + M_s) + (L_{sl} + 2M_{sl})(2\theta + 120^o)} \tag{35}$$

$$L_{Total-C} = \frac{3(L_s + M_s)^2 - \frac{3}{4}(2M_{sl} + L_{sl})^2}{2(L_s + M_s) + (L_{sl} + 2M_{sl})(2\theta - 120^o)} \tag{36}$$

This article has been accepted for publication in a future issue of this journal, but has not been fully edited. Content may change prior to final publication. Citation information: DOI 10.1109/ACCESS.2019.2912445, IEEE Access

Substituting (31)-(36) into (20)-(22), the ratios of the three phases can be expressed as

$$\overline{A}=\frac{(2L_s^{\,2}+4M_sL_s-\frac{3}{2}M_{sl}L_{sl}+2M_s^{\,2}-3M_{sl}^{\,2})}{3(L_s+M_s)^2-\frac{3}{4}(2M_{sl}+L_{sl})^2}+\frac{[(M_s+L_s)(M_{sl}-L_{sl})]\cos(2\theta)}{3(L_s+M_s)^2-\frac{3}{4}(2M_{sl}+L_{sl})^2}+\frac{[(2M_{sl}+L_{sl})(M_{sl}-L_{sl})]\cos^2(2\theta)}{3(L_s+M_s)^2-\frac{3}{4}(2M_{sl}+L_{sl})^2} \quad (37)$$

$$\overline{B}=\frac{(2L_s^{\,2}+4M_sL_s-\frac{3}{2}M_{sl}L_{sl}+2M_s^{\,2}-3M_{sl}^{\,2})}{3(L_s+M_s)^2-\frac{3}{4}(2M_{sl}+L_{sl})^2}+\frac{[(M_s+L_s)(M_{sl}-L_{sl})]\cos(2\theta+120^0)}{3(L_s+M_s)^2-\frac{3}{4}(2M_{sl}+L_{sl})^2}+\frac{[(2M_{sl}+L_{sl})(M_{sl}-L_{sl})]\cos^2(2\theta+120^0)}{3(L_s+M_s)^2-\frac{3}{4}(2M_{sl}+L_{sl})^2} \quad (38)$$

$$\overline{C}=\frac{(2L_s^{\,2}+4M_sL_s-\frac{3}{2}M_{sl}L_{sl}+2M_s^{\,2}-3M_{sl}^{\,2})}{3(L_s+M_s)^2-\frac{3}{4}(2M_{sl}+L_{sl})^2}+\frac{[(M_s+L_s)(M_{sl}-L_{sl})]\cos(2\theta-120^0)}{3(L_s+M_s)^2-\frac{3}{4}(2M_{sl}+L_{sl})^2}+\frac{[(2M_{sl}+L_{sl})(M_{sl}-L_{sl})]\cos^2(2\theta-120^0)}{3(L_s+M_s)^2-\frac{3}{4}(2M_{sl}+L_{sl})^2} \quad (39)$$

The cosine squared term is very small compared to the cosine term. Therefore, the ratios can be represented using sinusoidal approximations as given in (40)-(42).

$$\overline{A}\approx\overline{A1}=\frac{Y}{X}+\frac{Z}{X}\cos(2\theta) \quad (40)$$

$$\overline{B}\approx\overline{B1}=\frac{Y}{X}+\frac{Z}{X}\cos(2\theta+120^0) \quad (41)$$

$$\overline{C}\approx\overline{C1}=\frac{Y}{X}+\frac{Z}{X}\cos(2\theta-120^0) \quad (42)$$

where

$$X=3(L_s+M_s)^2-\frac{3}{4}(2M_{sl}+L_{sl})^2$$

$$Y=(2L_s^{\,2}+4M_sL_s-\frac{3}{2}M_{sl}L_{sl}+2M_s^{\,2}-3M_{sl}^{\,2})$$

and

$$Z=[(M_s+L_s)(M_{sl}-L_{sl})]$$

where $\overline{A}$, $\overline{B}$, and $\overline{C}$ are the ratios of phases A, B, and C to the DC bus voltage, respectively.

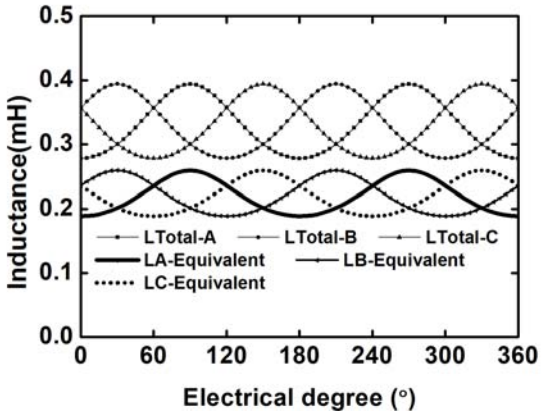

FIGURE 3A. Equivalent inductance and variations for phases A, B, and C.

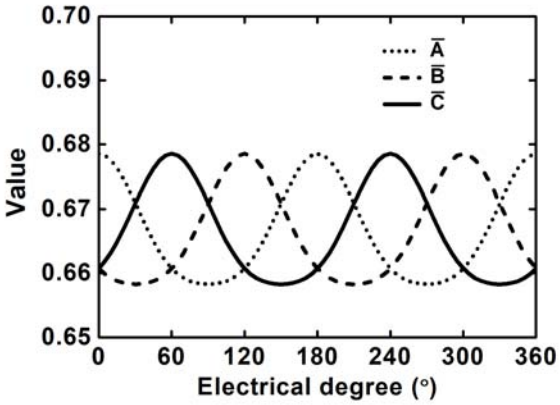

FIGURE 3B. Ratios for phases A, B, and C.

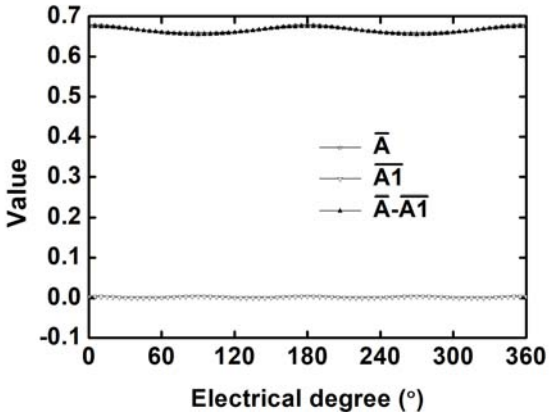

FIGURE 3C. Ratio and difference for phase A.

Equations (37)-(39) reveal the strong correlation between the motor rotor position and the detected neutral voltage. The proposed rotor position-detection method depends on this

relationship. During the motor starting phase, rotor polarity (i.e., 0°–180° or 180°–360°) is determined by injecting pulse voltage to motor stator windings in the *d–q* axis frame. Details of this process will be explained in the next section.

Figure 3a shows the equivalent inductance and variations obtained for phases *A*, *B* and *C*. Figure 3b shows the ratios of phases *A, B*, and *C* to the DC bus voltage. Figure 3c shows the variations in the ratio of $\overline{A}$, $\overline{A1}$ and the difference between $\overline{A}$ and $\overline{A1}$ for phase *A*, demonstrating that the difference between $\overline{A}$ and $\overline{A1}$ is small and can be neglected. This is also applicable for phases *B* and *C*.

B. SOFTWARE SOLUTION FOR NEUTRAL-VOLTAGE SCHEME

A software solution was implemented to verify the practicability of the neutral-voltage scheme. In the open loop, the motor was locked in different rotor positions. Sample voltages were obtained at the neutral point in different states at the rising edge of PWM. The neutral points of *A*, *B*, and *C* are the sample 12-bit digital values of the neutral voltages for phases *A*, *B*, and *C* in different states. Figures.4a and 4b show the sample values of the neutral voltages and neutral voltages/DC bus voltage ratios at different rotor positions.

It is clear that the neutral voltage of the motor varies significantly as the rotor position varies, as predicted by the outcome of the theoretical analysis shown in Fig.3. Figure 3 demonstrates the feasibility of the software solution for the neutral-voltage scheme for ratios of the neutral voltage to the DC bus voltage.

It is clear from equations (40), (41), and (42) that the position detection is based on the saliency of the variations of the difference between the self-inductance and the mutual inductance. The position detection scheme is not possible if L_{sl} is equal to M_{sl}.

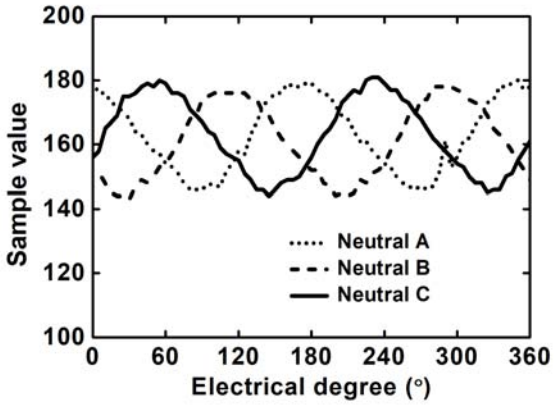

FIGURE 4A. Sample value of neutral voltage at different rotor positions.

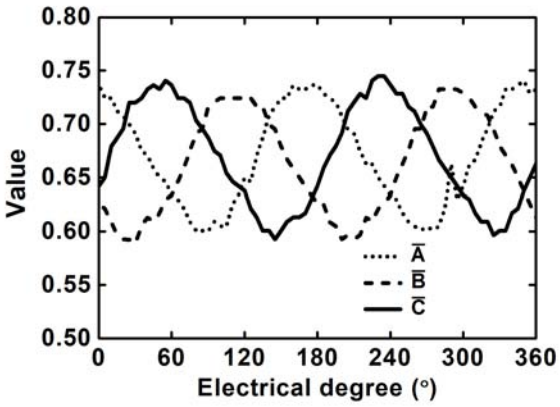

FIGURE 4B. Ratios of the neutral voltage to the DC bus voltage at different rotor positions.

The inductance ratios and the neutral voltage ratios are different, as the noise in the DC bus voltage and neutral voltages in the three states influence the accuracy.

C. NONLINEAR FLUX CHARACTERISTICS

Nonlinear flux characteristics were described in detail in [35]. Equation (43) gives the expression of the total flux linkage, where λ_{phase}, λ_{PM}, L, and i are the flux linkage of PMSM phase, the flux from the permanent magnet, the inductance of the energized phase, and phase current, respectively.

$$\lambda_{phase}=\lambda_{PM}+Li \tag{43}$$

In terms of variation in rotor position and phase current, (44) expresses the corresponding relationship between the inductance, current, and flux of the permanent magnet, where i^+ and i^-, L^+ and L^-, and $\Delta\lambda^+$ and $\Delta\lambda^-$ are the phase currents, inductances, and flux linkages corresponding to positive and negative pulse currents, respectively.

$$\begin{aligned} L^+ &= \frac{\lambda_{phase}-\lambda_{PM}}{i^+}=\frac{\Delta\lambda^+}{i^+} \\ L^- &= \frac{\lambda_{phase}-\lambda_{PM}}{i^-}=\frac{\Delta\lambda^-}{i^-} \end{aligned} \tag{44}$$

The absolute values of i^+ and i^- are equal. If $\Delta\lambda^-$ is larger than $\Delta\lambda^+$, L^- is correspondingly larger than L^+.

The voltage equation is expressed as (45), which describes the response of phase current to inductance variation.

$$v_s = Ri + L\frac{di}{dt} + e \tag{45}$$

where v_s, i, and e are the voltage, current, and back EMF of the phase, respectively. R and L are the resistance and inductance of the phase parameter, respectively in the three-phase reference frame.

As the back EMF is zero at standstill, phase current can be expressed by (46).

This article has been accepted for publication in a future issue of this journal, but has not been fully edited. Content may change prior to final publication. Citation information: DOI 10.1109/ACCESS.2019.2912445, IEEE Access

$$i = \frac{v_s}{R}(1 - e^{-\frac{R}{L}t}) \tag{46}$$

D. MORE PRECISE INITIAL ROTOR-POSITION SCHEME

1) INITIAL ROTOR-POSITION SCHEME

To improve the precision of the initial rotor position, vector pulses *V*1–*V*6 with the same width were correspondingly applied to detect sample resistor voltage. These pulses correspond to currents *I*1–*I*6 in the DC bus [31].

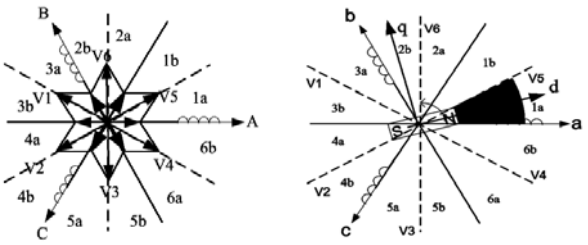

FIGURE 5. Initial rotor-position estimation. a) Voltage vectors; b) initial vector selection.

We extract maximum value I_{max} from the detected values of *I*1–*I*6 and determine matching voltage vector V_{max}, which can be applied to determine the initial position zone.

The values of *I*1–*I*6 were obtained, which represent the ratio of voltage vectors *V*1–*V*6 to the currents in the DC bus. We extract maximum value I_{max} from the detected values of *I*1–*I*6 and compare it with I_a, which follows I_{max}, and I_b, which precedes I_{max}. If $I_b > I_a$, the rotor is in the area between the magnetic field generated by V_{max} and V_b; otherwise, it is in the area between the magnetic field generated by V_{max} and V_a. As a result, the initial rotor position can be determined within a 30° resolution.

2) POLARITY IDENTIFICATION ON THE D–Q AXIS

$$\begin{cases} u_q = R_s i_q + pL_q i_q + \omega_r L_d i_d + e_0 \\ u_d = R_s i_d + pL_d i_d - \omega_r L_q i_q \end{cases} \tag{47}$$

In this study, a more precise initial rotor-position scheme was developed for permanent-magnet wheel motor (PMWM) applications. Equation (47) expresses the mathematical model of PMSM voltage on the *d*–*q* axis, where u_q, L_q, and i_q are the voltages, inductances, and currents on the *q* axis, respectively and u_d, L_d, and i_d are the voltages, inductances, and currents on the *d* axis, respectively.

At standstill, EMF (e_0) and angular speed (ω_r) are zero according to (47). If *q*-axis voltage (u_q) is zero, then *q*-axis current (i_q) is also zero.

$$T_e = \frac{3}{2}[\lambda_{PM} \times i_q + (L_d - L_q) \times i_d \times i_q] \tag{48}$$

Therefore, according to the expression for PMSM torque given in (48), the torque is zero.

$$\begin{cases} u_q = 0 \\ u_d = R_s i_d + pL_d i_d \end{cases} \tag{49}$$

We rearrange (47) as (49); thus, if *d*-axis pulse voltage (u_d) is injected, only *d*-axis current is developed, and no torque produced. We rearrange (46) as (50) on the *d*–*q* axis.

$$i_d = \frac{u_d}{R_s}(1 - e^{-\frac{R_s}{L_d}t}) \tag{50}$$

An increase in positive *d*-axis current causes the stator iron saturation and inductance on the *d* axis decreases, which can be applied to track the north pole of the rotor magnet [33].

The 360 electrical degrees are divided into six sections according to different voltage vectors. Fig. 6 shows the eight different rotor-position states at standstill. The rotor *d* axis is zero on the *a* axis shown in Fig. 6a. The rotor *d* axis is rotated by 180 electrical degrees on the –*a* axis shown in Fig. 6e.

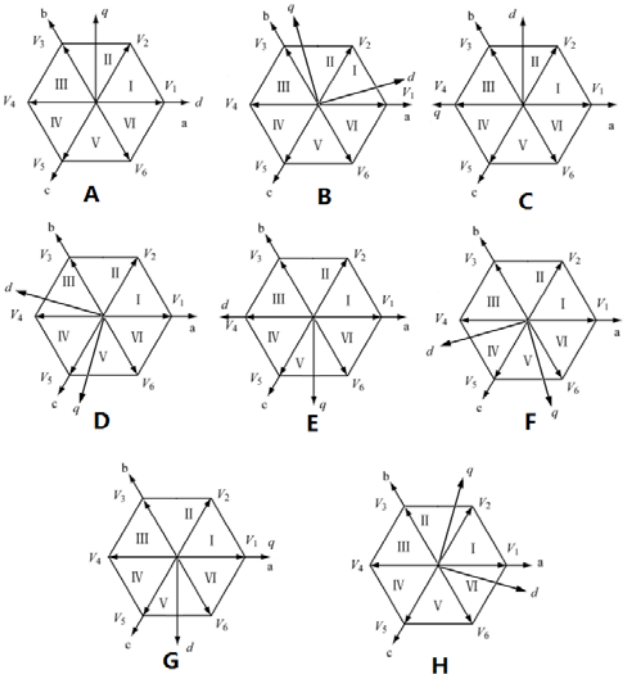

FIGURE 6. Diagram of the sections and basic voltage vectors at eight different positions.

In the *d*–*q* frame, where the neutral-voltage-based estimation method is applied, when the estimated electrical angle is close to zero or 180°, it is difficult to identify the polarity because the difference between the first and second current pulses is too small to be identified.

According to the correlation between phase *B* and the polarity at the moment of polarity change, it can be observed that the difference between the current pulses is sufficiently large to be identified. Thus, the current through phase *B* was employed instead of the current (i_d) through the *d* axis to identify polarity in this study.

This article has been accepted for publication in a future issue of this journal, but has not been fully edited. Content may change prior to final publication. Citation information: DOI 10.1109/ACCESS.2019.2912445, IEEE Access

When the current increases, the inductance decreases owing to the nonlinear characteristics of magnetic saturation, whereas when the current decreases, the inductance increases. When the higher current injection pulse is positive, the identified polarity corresponds to the north pole. Otherwise, the identified polarity corresponds to the south pole when the higher current injection pulse is negative.

Relative comparisons of the proposed position-detection technique are extremely advantageous. Angle error is approximately 5 electrical degrees. This result is comparable to that of the output position detection by the absolute encoder reported in [33].

III. SIMULATION OF POSITION DETECTION

A. SIMULATION OF POSITION DETECTION AT LOW SPEED

Angle output and angle error were determined by the S-function of the C code in MATLAB. Figs. 7a and 7b show the output results of the MATLAB simulation for an open loop. Figure 7a shows the relationship between the angle and angle error. The maximum angle error is 10 electrical degrees. The angle error is very large during motor starting without polarity identification.

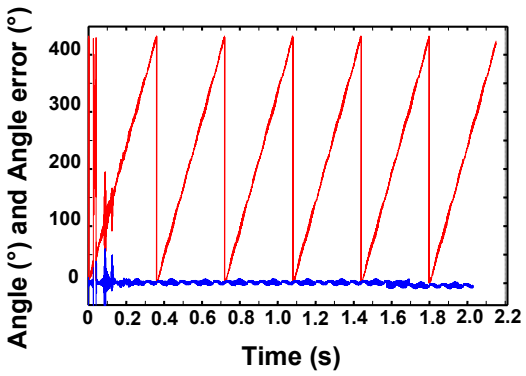

FIGURE 7A. Output angle (red) and angle error (blue) at 2.6 Hz on the carrier phase-shifted PWM.

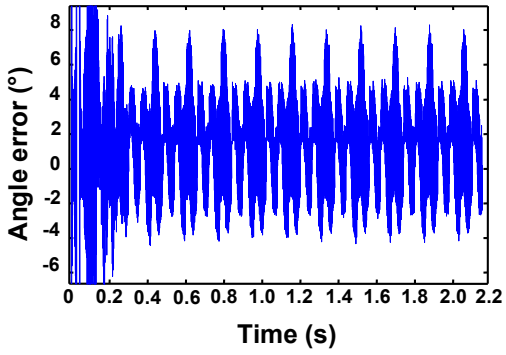

FIGURE 7B. Angle error at 2.6 Hz on the carrier phase-shifted PWM.

B. SIMULATION OF POSITION DETECTION BASED ON EMF

1) EFFECT OF BACK EMF

As the speed increases, the effect of the back EMF on the position detection is not negligible; thus, the angle error increases. For a three-phase motor, the phase-voltage equations are expressed as follows:

$$u_A - u_N = R_A i_a + \frac{di_a}{dt} L_a + \frac{di_b}{dt} M_{ab} + \frac{di_c}{dt} M_{ac} - e_A \tag{51}$$

$$u_B - u_N = R_B i_b + \frac{di_b}{dt} L_b + \frac{di_a}{dt} M_{ab} + \frac{di_c}{dt} M_{bc} - e_B \tag{52}$$

$$u_C - u_N = R_C i_c + \frac{di_c}{dt} L_c + \frac{di_b}{dt} M_{bc} + \frac{di_a}{dt} M_{ac} - e_C \tag{53}$$

where L_a, L_b, and L_c are the self-inductances of phases A, B, and C, respectively. M_{ab}, M_{ac}, and M_{bc} are the mutual inductances between phases A, B, and C, respectively. u_A, u_B, and u_C are the voltages of phases A, B, and C, respectively. u_N is the neutral voltage. i_a, i_b, and i_c are the currents in phases A, B, and C, respectively. e_A, e_B, and e_C are the back EMFs of the three phases in the motor.

2) SIMULATION OF POSITION DETECTION BASED ON EMF

Figure 8 shows the angle and angle error of the position detection of the EMF in the MATLAB simulation (open loop). The red line

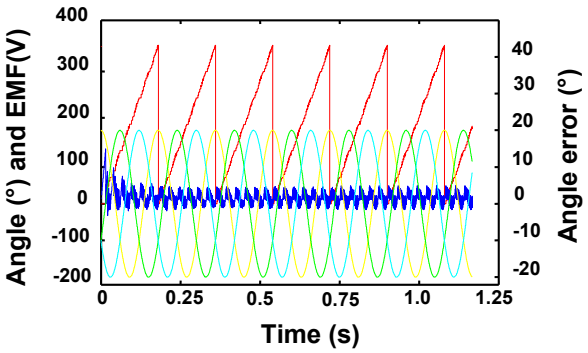

FIGURE 8A. Relationship between the theoretical EMF and angle output at 5 Hz.

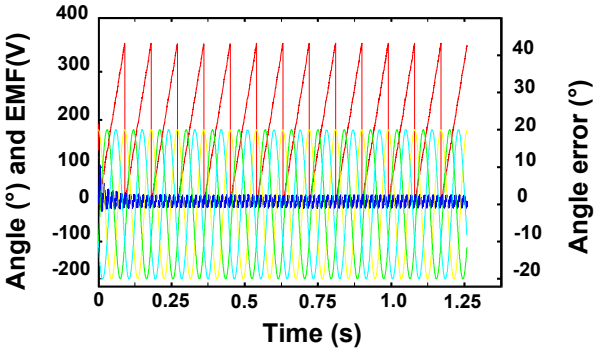

FIGURE 8B. Relationship between the theoretical EMF and angle output at 10 Hz.

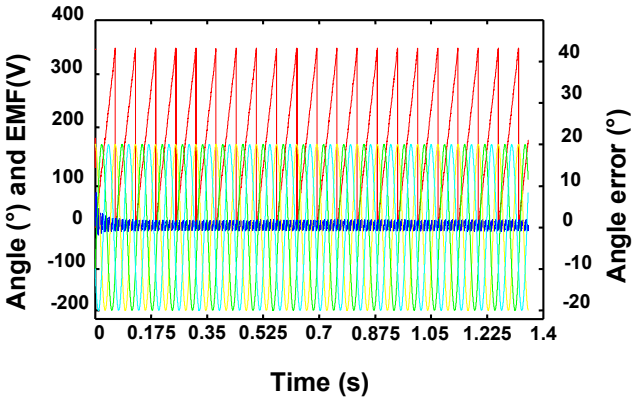

FIGURE 8C. Relationship between the theoretical EMF and angle output at 15 Hz.

represents the output angle. The blue line represents a comparison of the angle error and the ideal position, whereas the sinusoidal curve shows the output EMF.

The angle error shown in Figs. 8a, 8b, and 8c is approximately 10, 6, and 4.5 electrical degrees at 5, 10, and 15 Hz, respectively. The angle error of the position detection of the EMF decreases with an increase in the speed.

IV. EXPERIMENTAL RESULTS AND DISCUSSION

The experiment was conducted using 72-V DC batteries (Semikron IPM) and a 60-kW PMWM. The carrier frequency was 2 kHz. Table I lists the parameters of the wheel motor. XC161 was selected as the microcontroller unit (MCU) of the controller to perform position detection and control. The voltage signal was extracted from the position-detection technique using a divider resistor between the neutral point and DC bus ground, which was sampled three times in one phase-shifted PWM cycle at the rising edge. The 2θ value was extracted from (40)–(42) using a linear interpolation and a phase-locked loop, which can be derived from the sampled neutral voltages. The detected position of the controller was determined from the 2θ value and identified rotor polarity. The vector control function frame is given shown in Fig. 9, which includes the signal sample, position detection, d–q and inverse d–q transforms, and PWM inverter.

TABLE I
PARAMETERS FOR WHEEL MOTOR

Parameters	Value
pole pairs	23
rated motor power	60kW
inductance of L_q	1.357 mH
inductances of L_d	1.246 mH
stator resistance	0.045 Ω
rated voltage	550v

Details of software implementation of the position-detection are described elsewhere [33]. The neutral voltages were sampled to determine the electrical degree in the 0°–180° or 180°–360° zone. Then, the polarity in the *d*–*q*-axis frame is determined based on the electrical degree in the 0°–180° or 180°–360° zone. The output rotor position is expressed in terms of the electrical degrees in the 0°–360° zone in accordance with the polarity flag, which can be used to control motor starting in the *d*–*q*-axis frame.

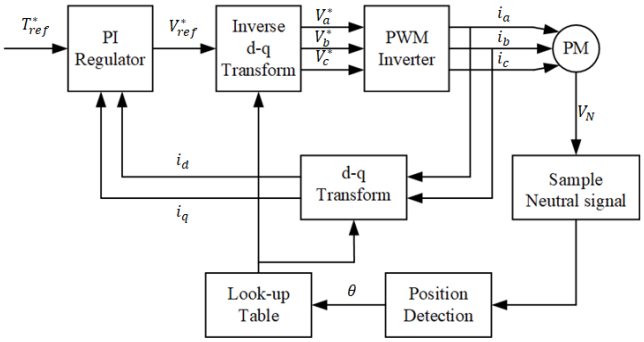

FIGURE 9. Function diagram of the position detection.

A. RESULTS OF THE POSITION DETECTION

The test device system operates under the condition of a 10-A current and 72-V DC bus voltage with a manual brake as load.

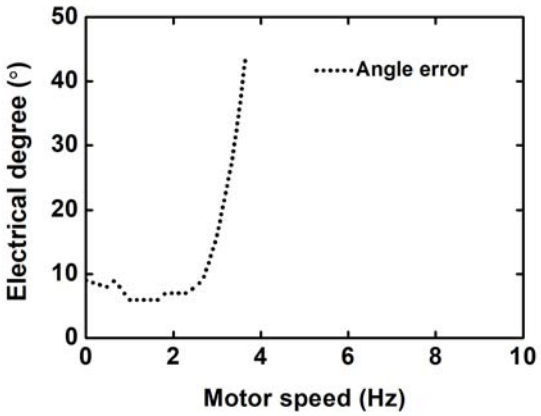

FIGURE 10. Angle error at different speeds.

The position-detection angle error from a standstill to low speed is shown in Fig. 10. The position-detection angle error represents the average angle when the motor operates in the stable state at each speed.

B. CHANGEOVER FROM LOW TO HIGH SPEED

Figure 11 shows the angle error of the detected position at different speeds. The position was determined in the open loop to extend the work range at different speeds. The crossover frequency of the different position-detection methods is approximately 3 Hz.

The changeover from low to high speed in the position-detection techniques can be performed using different methods. One of such methods is realized by changing the position-detection algorithm at the crossover point. The weighted-average method is another method used for the changeover. The simple average method is also used in the crossover zone.

Figure 12 shows weight coefficients $m1$ and $m2$. The detected velocity value obtained using the detected position determines the values of $m1$ and $m2$. The minimum and maximum speeds in the

changeover zone are determined at the minimum speed using the EMF method and determined at the maximum speed using the neutral-voltage method.

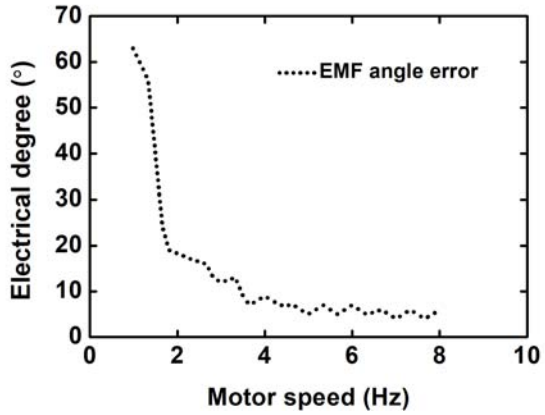

FIGURE 11A. Angle error of the position detection of the EMF at different speeds.

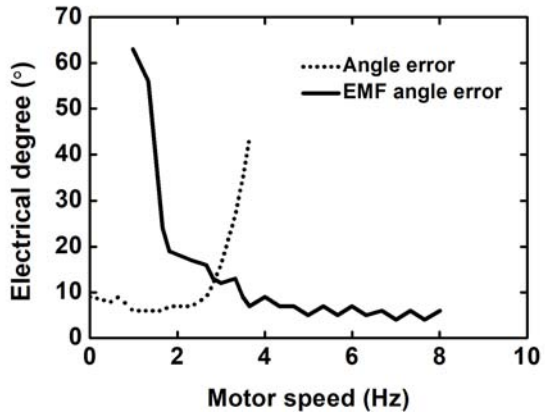

FIGURE 11B. Angle error of the position detection at different speeds.

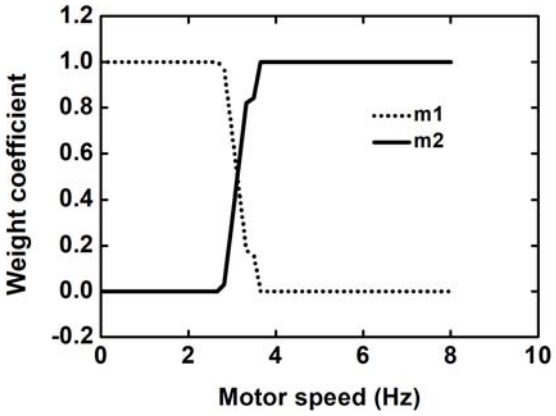

FIGURE 12. Weight coefficients obtained at different motor speeds.

A comparison of the angle error using different changeover methods is shown in Fig. 13. The angle error at the crossover point is smaller than of the changeover method. An adaptive hysteresis band is required at the crossover point when jumping, from low speed to high speed or vice versa, over the crossover point is necessary to swing the driver system.

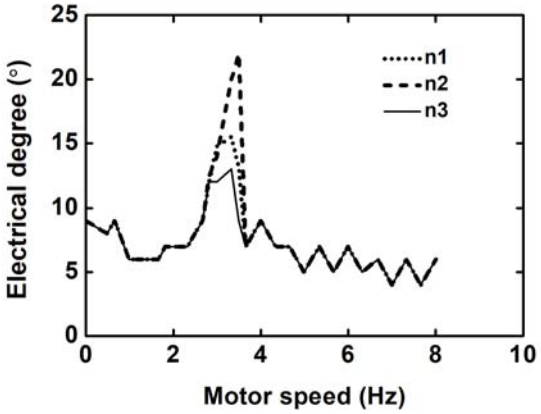

FIGURE 13. Angle-error comparison for different changeover methods.

C. EXPERIMENTAL STUDIES AT STANDSTILL

Lock the motor in different rotor positions, then make the encoder output as a reference for the mechanical scale and spin the rotor using 5° scale (electrical degree) in each step, which is a sample point. Record the output of the absolute encoder and the output of the position detection. The mechanical scales are used as the spinning reference. Figure14a shows a comparison of the outputs of the position detection and absolute encoder at standstill. The mechanical scales are divisions of the PMSM according to the pole pairs, which is used as reference when the rotor position varies. The output of the absolute encoder is used as reference for the rotor position, which is compared with the output of the position detection.

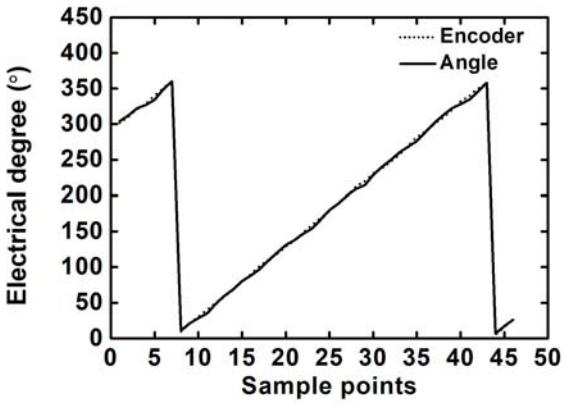

FIGURE 14A. Angle and encoder output at standstill

The angle error of position detection at standstill is shown in Fig.14b, which gives a comparison of the output position detection and the output of the absolute encoder. The angle error is approximately 6 electrical degrees.

This article has been accepted for publication in a future issue of this journal, but has not been fully edited. Content may change prior to final publication. Citation information: DOI 10.1109/ACCESS.2019.2912445, IEEE Access

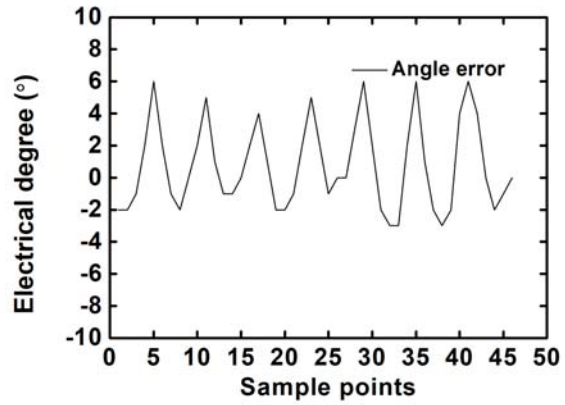

FIGURE 14B. Detection position angle error at standstill

D. STARTING-PROCESS EXPERIMENTAL STUDIES

An experimental power inverter and a control circuit board were built to control the PMWM for testing in the laboratory.

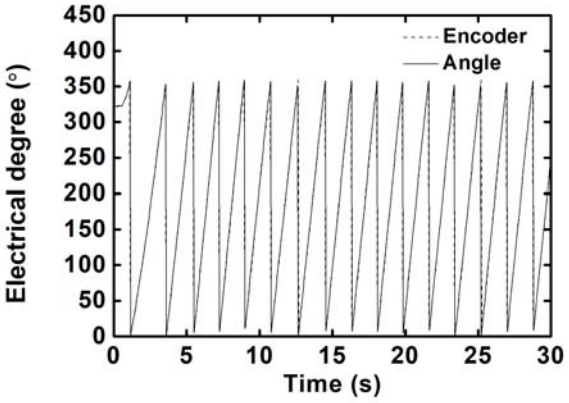

FIGURE 15A. Output angle of the position detection from standstill to a low speed.

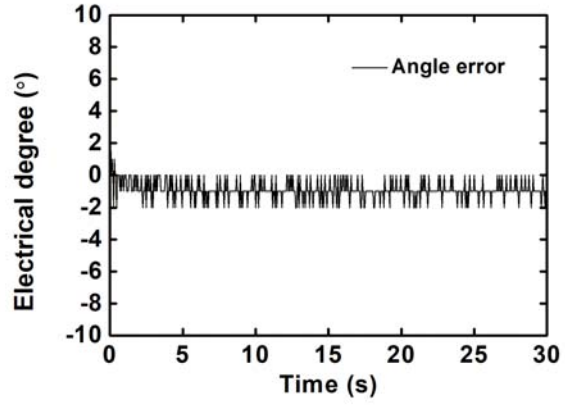

FIGURE 15B. Angle error between the detected angle and angle of the absolute encoder from standstill to a low speed.

The test device system was operated with a 2.5-A current and 72-V DC bus voltage using a manual brake for low-speed position detection. The detected output angle from standstill to low speed is shown in Fig. 15a. The detected angle error from standstill to a low speed (0.57 Hz) is shown in Fig. 15b. The maximum angle error detected was 3 electrical degrees.

Figure 16 shows the starting progress from standstill with 10-A current and 72-V DC bus voltage using a manual brake when the speed increases initially. The position angle and angle error are shown in Figs. 16a and 16b, respectively. The i_q current due to step demand in the motor torque is shown in Fig. 16 c, and the i_d current demand is zero. The i_q current is largely constant with small fluctuations caused by the manual brake load. The starting process from a standstill is shown in Fig. 16d, where there is gradual increase in the speed of the wheel motor, because a low current is applied to the wheel motor. The EMF flag denotes the state of the system operation based on EMF position detection. When the motor operates at a high speed, the EMF flag is one; otherwise, it is zero. Accordingly, the position is estimated using the neutral voltage.

The duty ratio at standstill is zero in Fig. 1b. The duty ratio is determined by torque control loop. The experimental results from a significantly lower duty ratio to a large duty ratio are presented for the different motor operation from standstill to high speed.

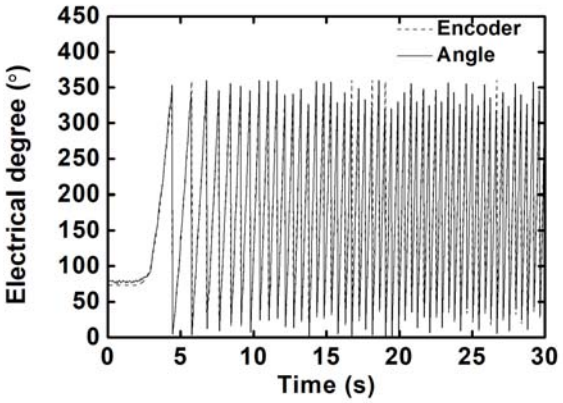

FIGURE 16A. Output angle of the position detection down to standstill.

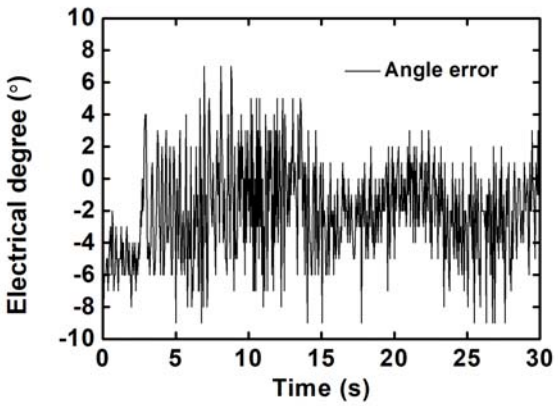

FIGURE 16B. Angle error between the detected angle and angle of the absolute encoder down to standstill.

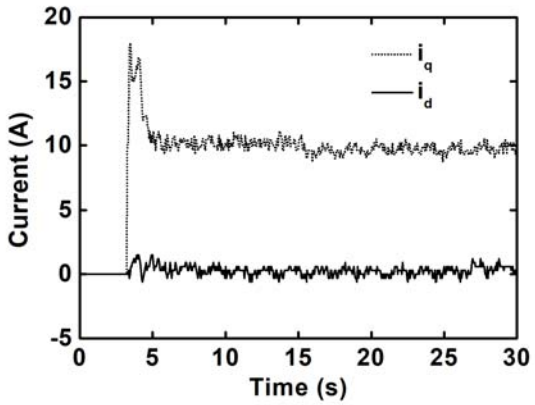

FIGURE 16C. **Start process from standstill with 10A current step response**

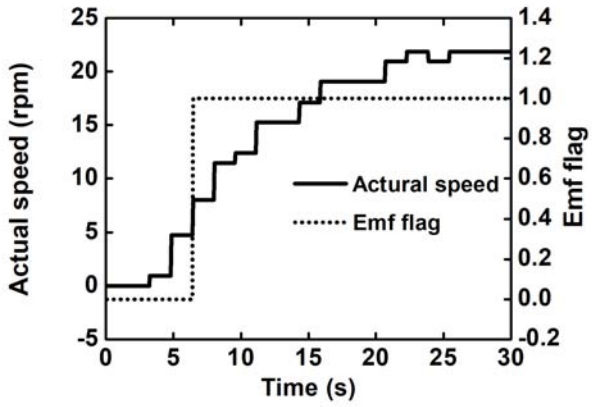

FIGURE 16D. **Start process from standstill and flag of the position detection of the EMF.**

V. CONCLUSIONS

An innovative PMWM rotor position-detection method based on carrier phase-shifted PWM is proposed. First, a detailed theoretical analysis of the PMWM neutral voltage was performed, then further verification processes, including simulation and experiment, were conducted to verify the strong correlation between the rotor position and the detected PMWM neutral voltage. This study exploited rotor polarity identification using the position-detection-based neutral voltage in the *d–q* axis owing to the saliency of the detected PMSM neutral voltage. Position detection using EMF was also simulated and verified by experiment, whereas the transition between the EMF-based and neutral-voltage-based position detection was achieved to ensure that the PMWM can smoothly start from standstill.

The experimental results of the proposed rotor position-detection method at standstill, low speed and from standstill to high speed were discussed. To verify the accuracy of the proposed position-detection techniques, the rotor-position angle error was derived and compared with the output of the rotor-position sensor. The proposed position-detection method was implemented using Infineon MCU XC161 to successfully drive a 60-kW PMSM from standstill to high speed.

The position-detection technique was implemented in the laboratory for the starting process from standstill to a low speed. In the future, we will include several operating progresses, such as full load and over load; anti-slip control; and a sudden/rapid increase in wheel speed with the existing torque control loop of the proposed rotor position-detection method.

SPWM (sinusoidal pulse width modulation) and SVPWM (space vector pulse width modulation) are two popular modulations for vector control. The proposed neutral voltage scheme is based on phase-shifted PWM with three PWM carrier waves (relative to phases *A*-*C* of the PMSM motor). The phase difference between adjacent modules must equal 120° as shown in Fig.1b. In transient conditions, six different circuit configurations are produced by shifting PWM in each switching cycle. The switching action for SVPWM is symmetrical in each PWM cycle so that it cannot result in six different circuit configurations in each cycle, i.e., the proposed position detection method is not possible for SVPWM. In the future, we plan to investigate the feasibility of the neutral voltage for SVPWM based on the different transient circuit configurations.

REFERENCES

[1] J. Johonson, M. Ehsani and Y. Guzelgunler. “Review of sensorless methods for brushless dc” IEEE Trans. Industry Application, vol.21. pp. 143-150, Oct 1999.

[2] E.K. Kenneth, A. C. Liew, and T. A. Lipo, “New observer-based DFO scheme for speed sensorless field-oriented drivers for low-zero-speed operation,” IEEE Trans Power Electron., vol.13. pp.958-968, Sept.1998.

[3] A. Consoli, A. Musumect, S. Raciti, and A. Testa “sensorless vector and speed control of brushless motor drive,” IEEE Trans. Ind. Electron., vol. 41, pp. 91-96, Feb.1994.

[4] F. Parasiliti, R. Petrella and M. Tursini, “Sensorless speed control of a PM synchronous motor based on sliding mode observer and extended Kalman filter” Proc. Of the Thirty Sixth IEEE-IAS Annual Meeting, Chicago, Sept. 30-Oct. 4, 2001.

[5] S. Bolognani, R. Oboe and M.Zigliotto, “Sensorless full-digital PMSM drive with EKF estimation of speed and rotor position” IEEE Trans. On Industrial Electronics, vol. 46, no. 1. pp. 184-191, Feb. 1999

[6] R. Dhaouadi, N. Mohan, and L. Norum, “Design and implementation of an extended Kalman filter for the state estimation of permanent magnet synchronous motor” IEEE Trans Power Electron., vol.6. pp.491-497, Sept./Oct. 1994

[7] X. Song; B. Han; S. Zheng; S. Chen “A Novel Sensorless Rotor Position Detection Method for High-Speed Surface PM Motors in a Wide Speed Range” IEEE Trans Power Electron., vol. 33, no. 8, pp.7083-7093 Aug. 2018

[8] W. Xu; Y. Jiang; C. Mu; F. Blaabjerg “Improved Nonlinear Flux Observer-Based Second-Order SOIFO for PMSM Sensorless Control” IEEE Trans Power Electron., vol. 34, no. 1, pp.565-579 Jan. 2019

[9] A. Consoli, G. Scarcella, and A. Testa, “Industry Application of Zero-Speed Sensorless Control Techniques for PM Synchronous Motors,” IEEE Trans. Ind. Application., vol. 37, no. 2, Mar./Apr. 2001.

[10] J.-H. Jang and S.-K. Sul, “Sensorless Drive of SMPM Motor by High Frequency Signal Injection,” in Proc. APEC 2002, Mar. 2002, pp. 279-285.

[11] D. Kaneko, Y. Iwaji, K. Sakamoto, and T. Endo, “Initial Rotor Position Estimation of the Interior Permanent-Magnet

Synchronous motor" Power Conversion Conference, PCC Osaka, vol. l, pp. 259-264, 2-5 Apr. 2002

[12] Yu-seok Jeong, Robert D. Lorenz, Thomas M Jahns and Seung-Ki Sul "Initial Rotor Position Estimation of an Interior Permanent-Magnet Synchronous Machine Using Carrier-Frequency Injection Methods" IEEE Traction on induction applications vol 41 no.1 pp. 38-45, Jan./Feb. 2005

[13] M. Schroedl, "Sensorless Control of AC Machines at Low Speed and Standstill based on the "INFORM" Method," in Conf. Rec. IEEE-IAS Annu. Meeting, Oct. 1996, pp.270-277.

[14] M. J. Corley, R. D. Lorenz, "Rotor Position and Velocity Estimation for a Permanent Magnet Synchronous Machine at Standstill and High Speeds," IEEE Trans. Ind. Application, vol. 34, no. 4, pp. 784-789, Jul./Aug. 1998.

[15] L. Harneforts, H. P. Nee, "A General Algorithm for Speed and Position Estimation of AC Motors," IEEE Trans. Ind. Electron., vol. 35, no. 1, pp.77-83, Feb. 2000.

[16] M. Linke, R. Kennel, and J. Holtz, "Sensorless Position Control of Permanent Magnet Synchronous Machines without Limitation at Zero Speed," in Proc. IECON'02, Nov. 2002, pp. 674-679.

[17] F. Parasiliti, R. Petrella, and M. Tursini, "Sensorless Speed Control of salient rotor PM Synchronous Motor based on High Frequency Signal Injection and Kalman Filter," in Proc. ISIE 2002, Jul. 2002, pp. 623-628.

[18] T. Kereszty, V.-M. Leppanen, and J. Luomi, "Sensorless Control of Surface Magnet Synchronous Motors at Low Speeds Using Low- Frequency Signal Injection," in Proc. IECON'03, Nov. 2003, pp. 1239-1243.

[19] X. Wu; Y. Feng; X. Liu; S. Huang; X. Yuan; J. Gao; J. Zheng "Initial Rotor Position Detection for Sensorless Interior PMSM With Square-Wave Voltage Injection" IEEE Trans. Magn., vol. 53, no. 11, pp. 1–4, Nov. 2017.

[20] H. Zhang; W. Liu; Z. Chen; G. Luo; J. Liu; D. Zhao "Asymmetric Space Vector Modulation for PMSM Sensorless Drives Based on Square-Wave Voltage-Injection Method" IEEE Trans. Ind. Appl., vol. 54, no. 2, pp. 1425–1436, Mar./Apr. 2018.

[21] Reiko Raute, Cedric Caruana, Cyril Spiteri Staines, Joseph Cilia, Mark Sumner, and Greg M. Asher, "Analysis and Compensation of Inverter Nonlinearity Effect on a Sensorless PMSM Drive at Very Low and Zero Speed Operation" IEEE Trans. Ind. Electron., vol. 57, no. 12, pp. 4065-4074, Dec. 2010

[22] Hongryel Kim, Jubum Son, and Jangmyung Lee"A High-Speed Sliding-Mode Observer for the Sensorless Speed Control of a PMSM" IEEE Trans. Ind. Electron., vol. 58, no. 9, pp. 4069-4077, Sept. 2011

[23] Sakorn Pongam and Somboon Sangwongwanich, "Stability and Dynamic Performance Improvement of Adaptive Full-Order Observers for Sensorless PMSM Drive" IEEE Trans Power Electron., vol. 27, no. 2, pp. 588-600, Feb. 2012

[24] Manu Jain, Mukhtiar Singh, Ambrish Chandra, and Sheldon S. Williamson "Sensorless Control of Permanent Magnet Synchronous Motor using ANFIS Based MRAS" IEMDC 2011 pp. 599-606,

[25] Angelo Accetta, Maurizio Cirrincione, Marcello Pucci, and Gianpaolo Vitale, "Sensorless Control of PMSM Fractional Horsepower Drives by Signal Injection and Neural Adaptive-Band Filtering" IEEE Trans. Ind. Electron., vol. 59, no. 3, pp. 1355-1366, Mar. 2012

[26] Amor Khlaief, Moussa Bendjedia, Mohamed Boussak, and Moncef Gossa "A Nonlinear Observer for High-Performance Sensorless Speed Control of IPMSM Drive" IEEE Trans Power Electron. vol. 27, no. 6, pp. 3028-3040, Jun. 2012

[27] Matteo Carpaneto, Paolo Fazio, Mario Marchesoni, and Gianluca Parodi "Dynamic Performance Evaluation of Sensorless Permanent-Magnet Synchronous Motor Drives with Reduced Current Sensors" IEEE Trans. Ind. Electron., VOL. 59, NO. 12, pp. 4579-4589, Dec. 2012

[28] Hyun Lee and Jangmyung Lee "Design of Iterative Sliding Mode Observer for Sensorless PMSM Control" IEEE Transactions on Control Systems Technology, vol. 21, no. 4, pp. 1394-1399, Jul. 2013

[29] Gaolin Wang, Tielian Li, Guoqiang Zhang, Xianguo Gui, and Dianguo Xu,"Position Estimation Error Reduction Using Recursive-Least-Square Adaptive Filter for Model-Based Sensorless Interior Permanent-Magnet Synchronous Motor Drives" IEEE Trans. Ind. Electron., vol. 61, no. 9, pp. 5115-5125, Sept. 2014

[30] Kwang-Woon Lee, Sungin Park, and Seongki Jeong "A Seamless Transition Control of Sensorless PMSM Compressor Drives for Improving Efficiency Based on a Dual-Mode Operation" IEEE Trans. Power. Electron., vol. 30, no. 3, pp. 1446-1456, Mar. 2015

[31] Hu, Hao; Xu, Guoqing; Hu, Bo "A New Start Method for Sensorless Brushless DC Motor Based on Pulse Injection" Asia-Pacific Power and Energy Engineering Conference, 2009

[32] Mei T X, Qu K W and Whitley M "Control of wheel motors for the provision of light rail traction and steering" UKACC International Control Conference, Coventry, UK, 7-10 Sept. 2010.

[33] Qu, Kewang; Xu, Guoqing; Zhou, Yimin; Yuan, Dengke; Hu, Hao "A novel standstill position detection method of PMSM for electric vehicles based on carrier phase-shifted PWM technology" IEEE International Symposium on Industrial Electronics, pp. 1594-1599, Jul. 24, 2014,

[34] Mei, T.X.; Qu, Kewang; Li, Hong "Control of wheel motors for the provision of traction and steering of railway vehicles" IET Power Electronics, vol. 7, no. 9, pp. 2279-2287, Sep. 1, 2014

[35] Kewang Q., Junci, C., Weili L., Yihuang, Z, Guoqing X., "PMSM Low Speed Position Detection on Carrier Phase-Shifted PWM Technology" 2016 IEEE Vehicle Power and Propulsion Conference, Proceedings, Dec. 19, 2016

KEWANG QU received the B.S. in Henan University of Science and Technology in 1997 and M.S. degrees in Tongji University in 2004 in electrical engineering. He has been working toward the Ph.D. degree in electrical engineering since 2012. His research interests include motor drives and control for electric vehicle applications.

WEILI LI was born in Harbin, China, in 1962. He received the Master's degree in 1993 in electrical machinery and appliance from the Harbin Institute of Electrical Technology, Harbin, and the Ph.D. degree in electrical machinery and appliance from Russia Electric Power Research Institute, Moscow, Russia, in 1997. He is the author or coauthor of more than 200 published refereed technical papers and he also holds 22 patents. He is currently a Professor at the College of Electrical Engineering, Beijing Jiaotong University, Beijing, China. His research interests include research on synthesis physical fields of large electrical machine and special electrical machine.

Dr. Li is an Editorial Board Member for the Journal of Electric Machines and Control. He is a Member of the International Compumag Society.

GUOQING XU received the B.Sc., M.Sc., and Ph.D. degrees from Zhejiang University, Hangzhou, China, in 1988, 1991, and 1994, respectively, all in electrical engineering. in 1997, he joined Tongji University, Shanghai, China, where he has been a Professor with the Department of Electrical Engineering since 2000. he has been a Director of the CAS-CUHK of SZ Advanced Integration Technology at the Chinese University of Hong Kong in 2010.Since 2016, he has been chief scientist of the Center for automotive electronics in Shenzhen Institutes of Advanced Technology, CAS, and a professor of Shanghai University. His research interests include electric vehicle control, motor drive and energy processing, and automotive electronics.

JUNCI CAO received the B.S. and M.S. degrees from the Harbin University of Science and Technology, Harbin, China, in 2001 and 2004, respectively, and the Ph.D. degree from the Harbin Institute of Technology, Harbin, in 2008, all in electrical engineering. He is currently an Associate Professor with the School of Electrical Engineering, Beijing Jiaotong University. His research interests include asynchronous traction drive system design, synchronous traction drive system design, simulation and reliability analysis, special motor design and integrated physical field research, motor optimization design, and system energy-saving projects.

T. X. MEI received the B.Sc. and M.Sc. degrees from Shanghai Tiedao University, Shanghai, China, in 1982 and 1985, respectively, the M.Sc. degree (by research) from Manchester University, Manchester, U.K., in 1991, and the Ph.D. degree from Loughborough University, Loughborough, U.K., in 1994. He currently holds the position of Chair in Control and Mechatronics at the School of Computing, Science and Engineering, Salford University, Salford, U.K. He was previously an academic (Lecturer in 2001, Senior Lecturer in 2003, and Reader in 2008) with the University of Leeds, Leeds, U.K. He is one of the most active researchers worldwide in the latest fundamental research into active steering and system integrations for railway vehicles. He has given many invited seminars and state-of-the-art reviews at the international level and has published more than 90 papers in the last ten years in leading academic journals and international conference proceedings. His main research is concerned with the advanced control and mechatronic solutions for industrial problems, particularly applied to railway and automotive systems, including fault tolerance, condition monitoring, traction control, wheel–rail contact mechanics, vehicle dynamics, intelligent sensing and data fusion, and system integration. Prof. Mei is a Chartered Engineer. He is a Fellow of the Institution of Engineering and Technology (U.K.).

ZHANG YIHUANG received the M.S. degree from the Harbin Institute of Electrical Technology, Harbin, China, in 1981. He is currently a Professor in the college of Electrical Engineering, Beijing Jiaotong University, Beijing, China. His research interests include research on the development of electric vehicle motor's system, electromagnetic properties, and loss of electrical materials.

HAO HU received the B.S. in electrical engineering and Ph.D. degrees in Vehicle operation engineering from Tongji University, Shanghai, China, in 2004, 2009 respectively. In 2009, he joined Tongji University, Shanghai, China, where he has been a lecturer in Institute of rail transit. His research interests include power electronics, vehicle control, motor drive and energy converting.